BIOPHYSICS

Active particles as mobile microelectrodes for selective bacteria electroporation and transport

Yue Wu[1], Afu Fu[2], Gilad Yossifon[1]*

Self-propelling micromotors are emerging as a promising micro- and nanoscale tool for single-cell analysis. We have recently shown that the field gradients necessary to manipulate matter via dielectrophoresis can be induced at the surface of a polarizable active ("self-propelling") metallodielectric Janus particle (JP) under an externally applied electric field, acting essentially as a mobile floating microelectrode. Here, we successfully demonstrated that the application of an external electric field can singularly trap and transport bacteria and can selectively electroporate the trapped bacteria. Selective electroporation, enabled by the local intensification of the electric field induced by the JP, was obtained under both continuous alternating current and pulsed signal conditions. This approach is generic and applicable to bacteria and JP, as well as a wide range of cell types and micromotor designs. Hence, it constitutes an important and novel experimental tool for single-cell analysis and targeted delivery.

INTRODUCTION

The exciting and interdisciplinary area of self-propelling or "active" particles (also termed micromotors) promises applications in drug delivery (*1*), detoxification (*2*), environmental remediation (*3*), immunosensing, remote surgery, self-repairing systems, self-motile devices, and more (*4*). Motion is achieved by designing particles that can asymmetrically draw and dissipate energy, creating local gradients of force for autonomous propulsion (*5*). With freedom to travel along individual pathlines, i.e., autonomous motion, active particles can cover larger areas and volumes and operate under simpler ambient conditions (i.e., without the necessity for field or chemical gradients) than phoretically driven particles. Active particles can be used for cargo transport (loading and translation on an active particle, i.e., "active cargo carrier") and delivery (release). To date, achieving both propulsion of the active carrier and cargo manipulation (load and release) has only been possible by combining two different mechanisms; self-propulsion can be driven by electric (*6*), magnetic (*7*), and optical (*8*) external fields (*9*) and even with chemical fuel (*10*), while cargo loading is achieved by magnetic, electrostatic (*11*), or biomolecular (*12*) recognition and attraction mechanisms. We recently demonstrated (*13*) a previously unstudied unification of carrier propulsion and cargo manipulation, demonstrating that it is possible to singularly control both processes by an applied external electric field. This unification allows notably simpler and more robust operation.

We have recently shown (*13*) that the field gradients necessary to manipulate matter via dielectrophoresis (DEP) can be induced at the surface of a polarizable, freely suspended active metallodielectric Janus particle (JP) under an externally applied electric field, acting essentially as a mobile floating microelectrode. The importance of this finding is that it offers a label-free method to selectively and dynamically manipulate (load, transport, and release) a broad range of organic and inorganic cargo. The DEP force (*14*) results from electric field gradients, generated locally at the carrier particle level, acting on the cargo particle–induced dipole. The DEP force can be either attractive (positive DEP) or repulsive (negative DEP), depending on the relative polarizability of the cargo compared to the medium, which is a function of the material's inherent electrical properties and the frequency of the applied field. Thus, high (low) electric field regions can be used to selectively trap particles exhibiting positive (negative) DEP.

Combining DEP with electrically powered active particle propulsion yields an active carrier that can selectively load, transport, and release a broad range of cargos, singularly controlled by an external electric field. Because of their facileness and controllability, we (*13*, *15*) and others (*5*, *16*) have focused on electric fields as a favorable source of energy for active particle propulsion. Electric fields enable the precise tuning of the induced propulsion forces on active particles in real time (*15*) and avoid issues of finite life and/or nonbiocompatibility of commonly used fuels, such as hydrogen peroxide (*17*). Furthermore, simple changes in the frequency of the applied electric fields can give rise to a number of distinct electrokinetic effects that can power locomotion in different ways. Uniquely, under the application of a uniform alternating current (AC) electric field, metallodielectric JPs (where one hemisphere is conducting and the other is dielectric) have been shown, by us and others, to respond as active particles (*15*, *18*), despite the external nature of the applied field. This distinctive feature arises from the propulsive mechanism, either induced-charge electrophoresis (ICEP) (*6*, *19*) or self-DEP (sDEP) (*15*), which is produced on the individual particle level rather than via an externally applied global gradient. It has the advantage of being fuel-free, and mobility is greatest in aqueous electrolytes. The addition of magnetic steering, e.g., magnetizing a ferromagnetic Ni layer coated on half of the JP surface (*20*) and using an external rotating static magnet, enables directed motion and selective trapping of cells.

Electrical-, ultrasonic-, chemical-, and mechanical-based lysis of *Escherichia coli* in microfluidic systems has been reviewed by Brown and Audet (*21*). Electrical lysis of cells (i.e., irreversible electroporation) is commonly performed with large electrodes in a batch mode for the treatment of a large number of cells, e.g., the microfluidic devices developed by Hügle *et al.* (*22*) and Vulto *et al.* (*23*). Because of the commonly large gap (~6 to 10 mm) between the electrodes, a relatively high voltage (~280 V) is required. Reduction of the applied voltage is possible by electric field intensification, obtained by either a microscale gap between the electrodes (*24*), singular-like geometries

[1]Faculty of Mechanical Engineering, Micro- and Nanofluidics Laboratory, Technion–Israel Institute of Technology, Haifa 32000, Israel. [2]Technion Integrated Cancer Center, Rappaport Faculty of Medicine and Research Institute, Technion–Israel Institute of Technology, Haifa 3109602, Israel.
*Corresponding author. Email: yossifon@technion.ac.il

[e.g., multiscale electrodes, nanopillar electrodes (*25*), and saw-tooth electrodes (*26*)], or micropore array–based (*27*) or nanochannel array–based electroporation (*28*). These local electric field intensification approaches allow single-cell electroporation (*24*), which opens up new opportunities in manipulating the genetic, metabolic, and synthetic contents of single targeted cells. However, these techniques perform electroporation on the cells that are randomly brought to the regions (i.e., electrodes and pore) of intensified electric field and lack the ability to selectively electroporate specific cells.

To perform selective electroporation of cells, Lundqvist *et al.* (*29*) used solid carbon fiber microelectrodes, which are mounted on a micromanipulator, to selectively trap and electroporate single cells. More recently, Nadappuram *et al.* (*30*) developed a nano-tweezer, which consists of two closely spaced electrodes, with gaps as small as 10 to 20 nm, to extract single molecules/organelles from living cells. Micropipette techniques (*31*) can also perform selective trapping and electroporation. Besides the complexity of fabrication of these electrodes with a nanometer-scale gap, these techniques require high-precision micromanipulators with free access from the outside to the sample and hence can be considered "invasive" techniques. In contrast, the micromotor can be applied in closed microfluidic chambers and externally controlled using electric and magnetic fields. Such a design offers inherent intensification of the electric field due to the nanometer gap between the floating metallic patch and the conductive substrate. Together with its directed motion ability, using magnetic steering, our approach, using the active particle as a mobile microelectrode, offers a substantially simplified and efficient method of unifying selective trapping and electroporation of cells, singularly controlled via an externally applied electric field.

JP propulsion and cargo manipulation must be operated under AC electric field conditions within the parallel indium tin oxide (ITO)–coated glass slide setup to suppress the generation of the gas bubble products of the faradic reactions on the electrodes (*26*). Although direct current (DC) pulses are the dominant electroporation mode (*32*), continuous AC fields have also been reported to cause cell electroporation and lysis (*33*). Here, we demonstrate that the locally intensified electric field intensity and gradient at the JP level enable both selective collection of *E. coli* and effective electroporation of the cells, with a moderate voltage, using either a continuous AC field or a train of pulses for electroporation. A significantly higher electroporation rate was observed for *E. coli* collected by JPs, relative to untrapped *E. coli*, proving that our micromotor-based approach enables targeted electroporation of cells. Hence, in the current study, we extend the application of the JP beyond that of a cargo carrier (*13*) to a platform for local electroporation of selectively trapped cells.

RESULTS

Directed motion–based selective trapping and release

To study *E. coli* trapping using a metallodielectric Janus sphere in an experimental setup consisting of conductive (ITO-coated glass slides) top and bottom substrates, we performed a *z* scan (11 planes within 10-μm distance from ~2 μm below the substrate) of the JP (see Fig. 1, C and E). It was found that *E. coli* were trapped at two locations: (i) between the ITO slide and the metallic side of the JP and (ii) at the equator of the polystyrene side of the JP. This is in qualitative agreement with the numerical simulation results indicating that the strongest electric field and field gradients are formed in the inherent small gap between the metallic side of the JP and the wall, with smaller field and field gradients also observed at the equator of the dielectric hemisphere (Fig. 1, D and F). As a result, we observed trapping due to positive DEP at these locations. The DEP response of both live and dead bacteria at the low solution conductivity (σ~9 μS/cm) at which the experiments were conducted is expected to be positive (*34*) and was verified by us using the quadrupolar electrode array (see fig. S1). At low frequencies (~30 kHz), AC electroosmotic flow dominated the response. It should be noted that, in some cases, bacteria were also trapped above the JP because of positive DEP resulting from the local large electric field gradients existing at the metallodielectric interface (Fig. 1, D and F). However, our region of interrogation (i.e., between planes A-A and B-B) was below the top of the JP as we were focused on visualizing only those trapped at or below the equator of the JP.

It was also found that the orientations of the *E. coli* trapped in between the metallic side of the JP and the bottom substrate were distinctively different in low and high frequencies. In the low-frequency regime (50 ± 20 kHz), the metallic side of the JP was partially screened because of the induced electrical double layer (EDL). Therefore, the electrical field outside the EDL had a nonzero tangential electric field component along which the trapped *E. coli* aligned and seemed to be "standing up" (i.e., with its major axis normal to the ITO substrate) (Fig. 1A). However, at higher frequencies (5 MHz), much beyond the relaxation time of the induced EDL [$f_{RC} = 1/2\pi\tau \sim 1.6k$ Hz (*35*); where $\tau = \lambda a/D$ is the induced charge relaxation, $\lambda = \sqrt{\varepsilon D/\sigma} \sim 40$ nm is the Debye length, $a = 5$ μm is the radius of the JP, $D \sim 2 \times 10^{-9}$ m^2/s is the diffusion coefficient of the ionic species (*36*), σ~9 μS/cm is the measured conductivity of the solution before introduction of the *E. coli*, $\varepsilon \sim 80\varepsilon_0$ is the permittivity of water, and ε_0 is the permittivity of the vacuum], there was not sufficient time for charging of the induced EDL; hence, the electrical field lines were perpendicular to the nonscreened metallic hemisphere. In this case, to fit into the small gap between the JP and the wall, the *E. coli* had to "lie down" (i.e., with its major axis parallel to the ITO substrate) (Fig. 1B).

The reason for choosing these two frequencies (50 ± 20 kHz and 5 MHz) for studying the continuous AC electroporation was because the JP propulsion velocity at these frequencies approximately vanished (Fig. 2C; see also movie S1), which facilitated confocal *z*-scan imaging at a fixed location. The low-frequency regime (50 ± 20 kHz) corresponds to the critical frequency at which the JP reverses direction from ICEP to sDEP motions. This critical frequency depends on the local conductivity of the solution (*15*), which might be affected by cytoplasm coming out from the electroporated cells, and hence varies within a range of frequencies. However, because of the low concentration of the bacteria in the solution, it is not expected to be a strong effect in terms of both conductivity and molecule adsorption on the JP surface. The exact value of the frequency at which the JP velocity vanishes, which also determines the continuous AC field electroporation conditions, then needs to be determined for each test. The sequential stages of trapping, electroporation, and release are described in Fig. 2 (A and B) (see movies S2 and S3). The JP first collected *E. coli* in the ITO chamber (300 kHz and 10 V, 2 min), moving at a velocity of ~20 μm/s, which is around the maximum velocity achieved in the sDEP mode (Fig. 2C). After 2 min of trapping, the electrical field parameters were changed to the desired continuous AC field electroporation conditions. As a result, the outer layer of the trapped *E. coli* became untrapped (weak DEP force relative to thermal motion)

and diffused away. Propidium iodide (PI) uptake by *E. coli* was used as an indication of membrane electroporation (*37*). The electroporation efficiency, defined as the ratio of the number of electroporated cells relative to the total number of trapped cells, was below 10% during the trapping stage, which suggests the ability to carry intact biological matter and electroporate it at a second location.

As the voltage increased, the number of *E. coli* trapped between the JP and the ITO substrate and on the equator of the polystyrene side also increased (Fig. 2D), as was expected because of the increased DEP force (*13*). In the low-frequency case (50 ± 20 kHz), the number of trapped *E. coli* increased with time. This was due to the induced-charge electro-osmotic flow (*35*) generated at the metallic hemisphere in the form of jetting, which brought more *E. coli* from the polystyrene side of the JP (see movie S4 and fig. S2). In contrast, in the high-frequency case (5 MHz), where there was no electroconvection because the frequency was substantially higher than the resistor-capacitor frequency of the induced charge, the number of *E. coli* trapped at the JP remained unchanged.

During the release stage (i.e., electric field is turned off), a large number of *E. coli* that were trapped above the JP but could not be visualized during the field operation were released. Hence, in this work, we only studied the electroporation efficiency of the *E. coli* trapped between the JP and ITO substrate as well as those trapped at the equator of the polystyrene side, as these could be visualized during the entire process.

Local and selective electroporation under continuous AC field

Figure 3 depicts the micrographs of the PI-stained *E. coli* within the ITO chamber under various AC field parameters and operation times. As expected, the PI uptake for trapped *E. coli* increased with the voltage because of the increased voltage drop across the cell membrane (i.e., transmembrane potential $\Delta\psi_{membr}$), which, in turn, resulted in increased electroporation (*38*), in accordance with Schwan's equation (*39*).

PI uptake rate was significantly higher in the trapped versus untrapped *E. coli*. For example, under low frequency (50 ± 20 kHz and 10 V) (Fig. 3), 80% of the trapped *E. coli* were stained at 10 min, whereas most of the untrapped *E. coli* were still intact (20% PI uptake). Under high frequency (5 MHz and 10 V) (Fig. 4), 45% of the trapped *E. coli* were stained at 10 min, whereas only ~18% of the untrapped *E. coli* were stained. However, while at high frequency, PI uptake increased monotonically with increasing voltage; at low frequency, PI uptake at 5 V was higher than at 15 V from 4 to 17 min (Fig. 3). This unexpected result might partly stem from the fact that there were multiple layers of *E. coli* trapped at 15 V (see also the transition from a single layer to multiple layers of trapped polystyrene 2-μm particles upon increase of the voltage from 5 to 15 V, as depicted in fig. S2), where the bacteria located at the outer layers were less affected by the intensified electric fields as they were located further away from the center of the JP and because the electric fields were screened by the cells within the inner layers. In addition, the induced electroconvective flow generated by the metallic hemisphere of the JP may have continuously pumped intact *E. coli* from the bulk region from the JP dielectric side. Furthermore, the PI uptake rate of trapped *E. coli* at high frequency was lower than at low frequency. For example, at 5 V, up to ~75% of the cells were stained at the high frequency (Fig. 4) and 100% at low frequency (Fig. 3). This is expected, as the transmembrane potential decreased with increasing frequency (*26*), according to Eqs. 2 and 3 (see table S1).

Viability test of local and selective electroporation under continuous AC field

Here, we used 6-carboxyfluorescein diacetate (CFDA) (*40*) and PI-stained *E. coli* to prove that our micromotor enables both reversible (i.e., cell viability is retained) and irreversible (i.e., electrical lysis of cells) electroporation. While PI is an indication of electroporation, CFDA is an indication of cell viability. As shown in Fig. 5 (A and B), while the fluorescence intensity of PI increases, the fluorescence intensity of CFDA decreases for both low- and high-frequency electroporation, indicating that cell viability is decreasing during the electroporation process. PI increased faster in low-frequency (33 kHz) electroporation than in high frequency (5 MHz), while CFDA decreased similarly at both frequencies. This result further confirms that electroporation efficiency is strongly dependent on the frequency and is more efficient at the lower frequency. In contrast, cell death seems to be less dependent on the frequency. As shown in Fig. 5C, a successful reversible electroporation of PI was achieved (>50% intake efficiency) without inducing notable *E. coli* damage, as revealed by ~80% CFDA retention when the electroporation is conducted at 33 kHz and 10 V for less than 1 min.

Local and selective electroporation under AC pulses

To suppress continuous electroporation while holding the bacteria, it is preferred to use high frequency, which maintains a lower transmembrane potential (e.g., 5 MHz instead of 50 ± 20 kHz). In this manner, on-demand electroporation can be achieved by combining short pulses (*41*) with a continuous AC signal. Moreover, the electroconvection flow that occurs under the low-frequency regime and may adversely influence the cell status (e.g., bringing new bacteria and shearing trapped bacteria) is completely suppressed. When applying an AC pulse train, the JP remained on the substrate in contrast to the case of DC pulse, which seemed to levitate the JP and, in this manner, lose the trapped cells. In addition, AC signals tend to reduce electrolysis relative to DC signals (*41*). As shown in Fig. 6, application of a train of 10 AC pulses (see movie S5) yielded a significantly higher percentage of PI-stained cells (100%) compared with a train of 5 (25%) or 1 (15%) AC pulse applied over the same incubation time (4 min). Moreover, after 10 pulses and 4 min of incubation, most of the untrapped *E. coli* were still intact (<25% PI uptake). It should be noted that we made no attempt to optimize the parameters (e.g., duration, peak intensity, and interval between pulses) of the pulses and still obtained a clear differentiation in the electroporation response between the conditions at the JP versus the untrapped *E. coli*. These parameters can be tuned in the future when reversible or nonreversible electroporation conditions are required.

DISCUSSION

An electrokinetically driven JP can function as a mobile microelectrode, capable of manipulating cargo via DEP, and serve as a platform for electroporation of cells due to locally intensified electrical field. In this work, we successfully unified the selective transport, loading, and electroporation of biological cargo by changing the frequency and amplitude of the applied electric field.

Regarding the trapping capacity of the JP, it was shown that at a frequency of 300 kHz, the number of trapped *E. coli* increased with increasing voltage, as expected, and in agreement with our previous results of JP trapping of polystyrene particles (*13*). The *E. coli* trapped

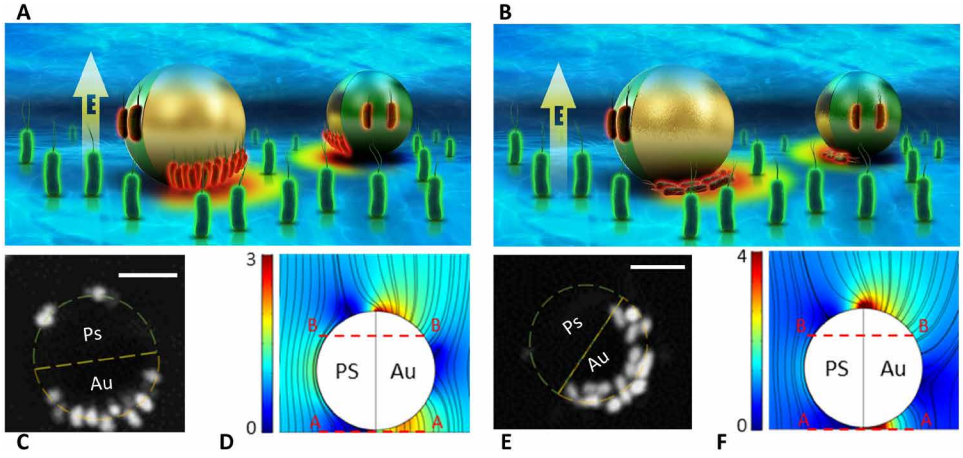

Fig. 1. Selective bacteria trapping and electroporation. Schematic illustrations of selective bacteria transport and electroporation using a JP as a mobile microelectrode and a continuous AC electric field are shown. The *E. coli* potentially trapped above the JP are not depicted in (**A**) and (**B**), as we were focused on visualizing only those trapped at or below the equator of the JP. (A, **C**, and **D**) 50 ± 20 kHz and 15 V. (B, **E**, and **F**) 5 MHz and 15 V. (C and E) Confocal microscopy images obtained by projection of *z* scans from plane A-A to B-B [as shown in (D) and (F)]. The bacteria that are trapped below the JP exhibit a distinct orientation at low and high electric field frequencies. (D and F) Electric field surface plots and streamlines, as obtained from numerical simulations for low ($f/f_{RC} = 3$) and high ($f/f_{RC} \gg 1$) frequencies. Scale bars, 5 μm.

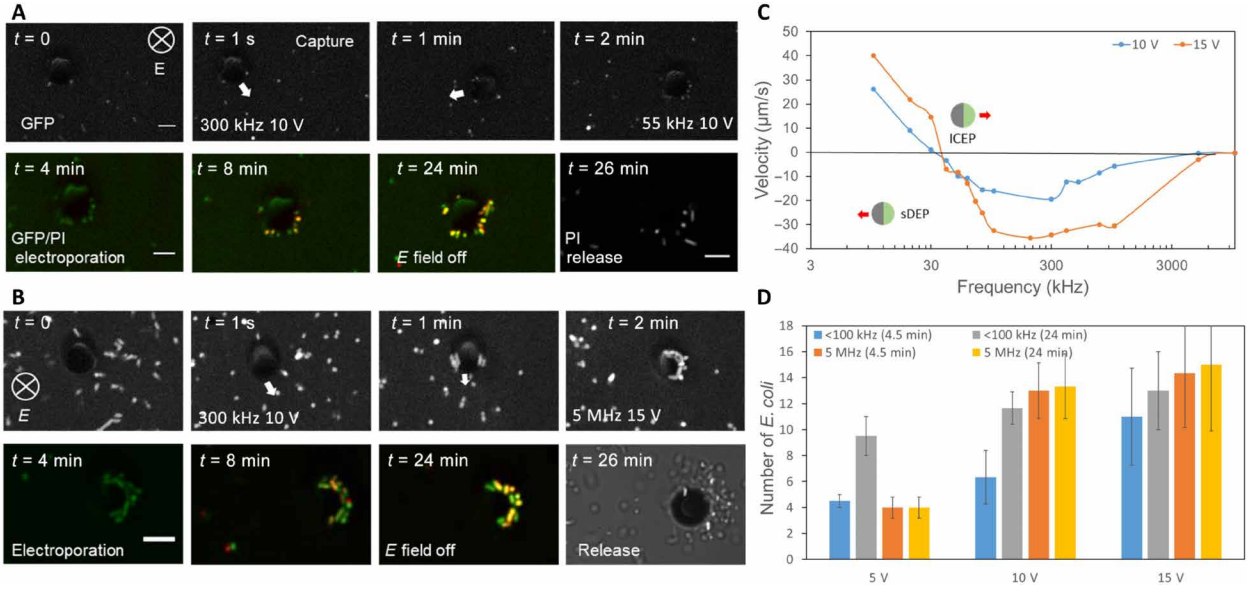

Fig. 2. Sequential trapping, electroporation, and release of *E. coli*. Trapping was conducted at 300 kHz and 10 V, with a moving JP, while electroporation was performed at either (**A**) 50 ± 20 kHz (see movie S2 and fig. S3) or (**B**) 5 MHz (see movie S3), where the JP was immobile, as evident from (**C**), depicting the JP particle velocity versus frequency (see movie S1). The applied voltage in the electroporation stage varied, but results of the case of 10 and 15 V are shown here. (**D**) Number of *E. coli* trapped between the JP and the ITO glass, including at the JP equator, at the low (50 ± 20 kHz)- and high (5 MHz)-frequency regimes, for different operation times, and varying voltages. Error bars represent SD computed from three independent tests. Scale bars, 5 μm.

at low frequency versus high frequency showed distinct orientations resulting from the different electric field streamlines obtained under the different frequency regime. This observation was due to the nonspherical (rod) shape of the bacteria, in contrast to the previously studied spherical polystyrene particles. Essentially, at frequencies much lower than the relaxation frequency of the induced electric double layer (EDL), the metallic hemisphere is electrically screened and the electric field lines outside the EDL are mostly tangential to the JP surface, resembling the electrostatic solution around an insulator. At very high frequencies, wherein there is not sufficient time for the charging of the induced EDL, the metallic hemisphere is not screened and the electric field lines are perpendicular to it, resembling the electrostatic solution around a conductor.

The most important finding of the current study was the ability of the JP to selectively electroporate the trapped cells due to the local electric field intensification, induced by the JP itself, at two locations: (i) under the metallic surface and (ii) at the equator of the polystyrene surface. Electroporated cells were stained with PI, and their percentage increased with increasing voltages, at all frequencies. Moreover, for the same applied voltage, the PI uptake rate was higher at the lower

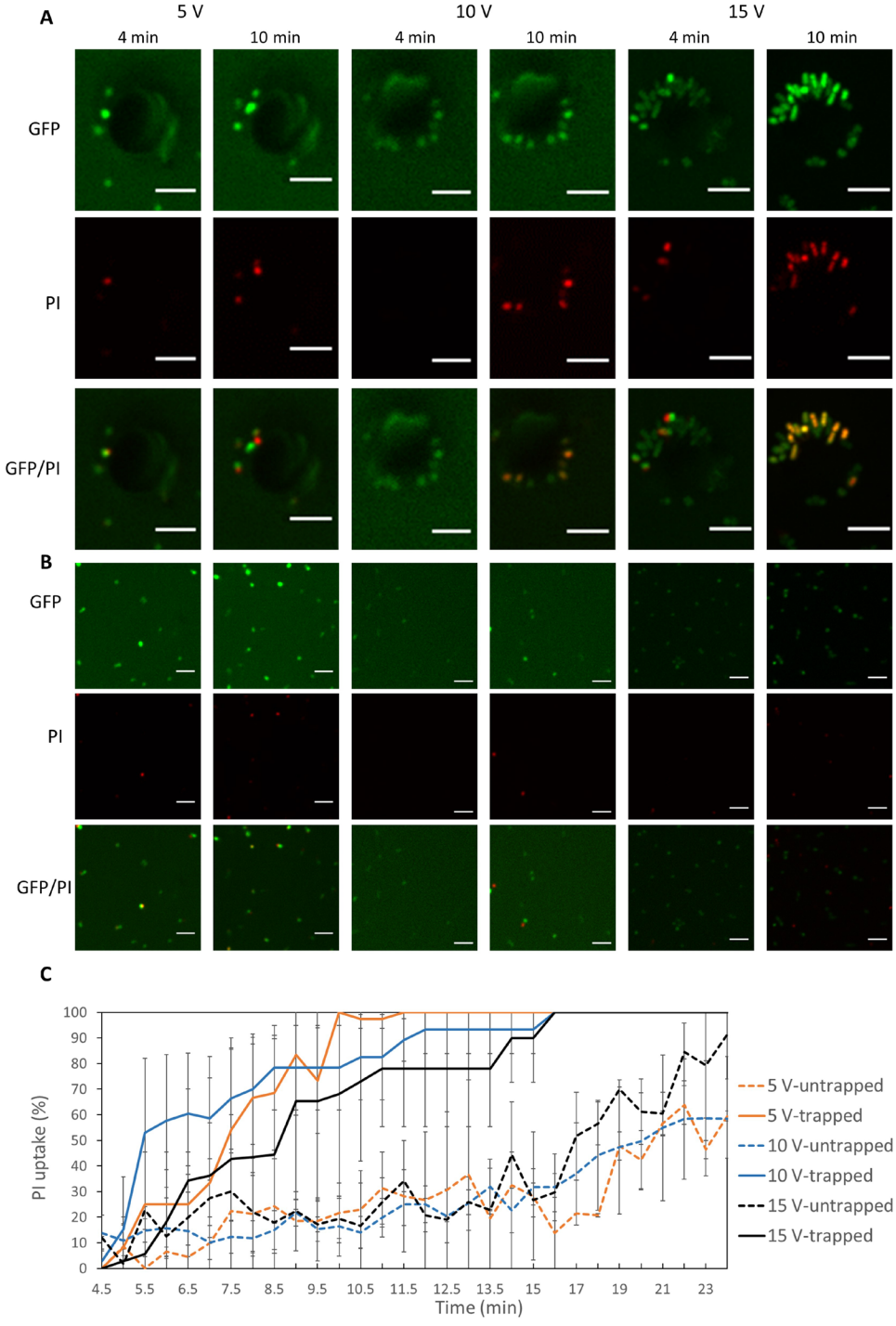

Fig. 3. Microscopy images of PI-stained trapped versus nontrapped *E. coli* at low frequency (50 ± 20 kHz), various applied voltages, and operation times. PI uptake (red fluorescence) indicates cell electroporation. Microscopic images of (**A**) trapped *E. coli* and (**B**) untrapped *E. coli*. (**C**) Percentage of both trapped and untrapped PI-stained *E. coli* over time at various applied voltages (~33 kHz). Error bars represent SD computed from three independent tests. JP of 10 μm in diameter was used. *E. coli* strain XL1-Blue bacteria with GFP labeling were used. Scale bars, 5 μm.

frequency (50 ± 20 kHz), in agreement with the Schwan's equation (*39*) for the transmembrane potential. It was found that at the end of the trapping stage (2 min), less than 10% of the trapped cells were electroporated, which enabled the collection and transport of intact *E. coli* to a secondary location, where they were then electroporated and further analyzed.

Because both DEP and electroporation apply to any type of cell (regardless of its size, shape, and surface properties) and are not

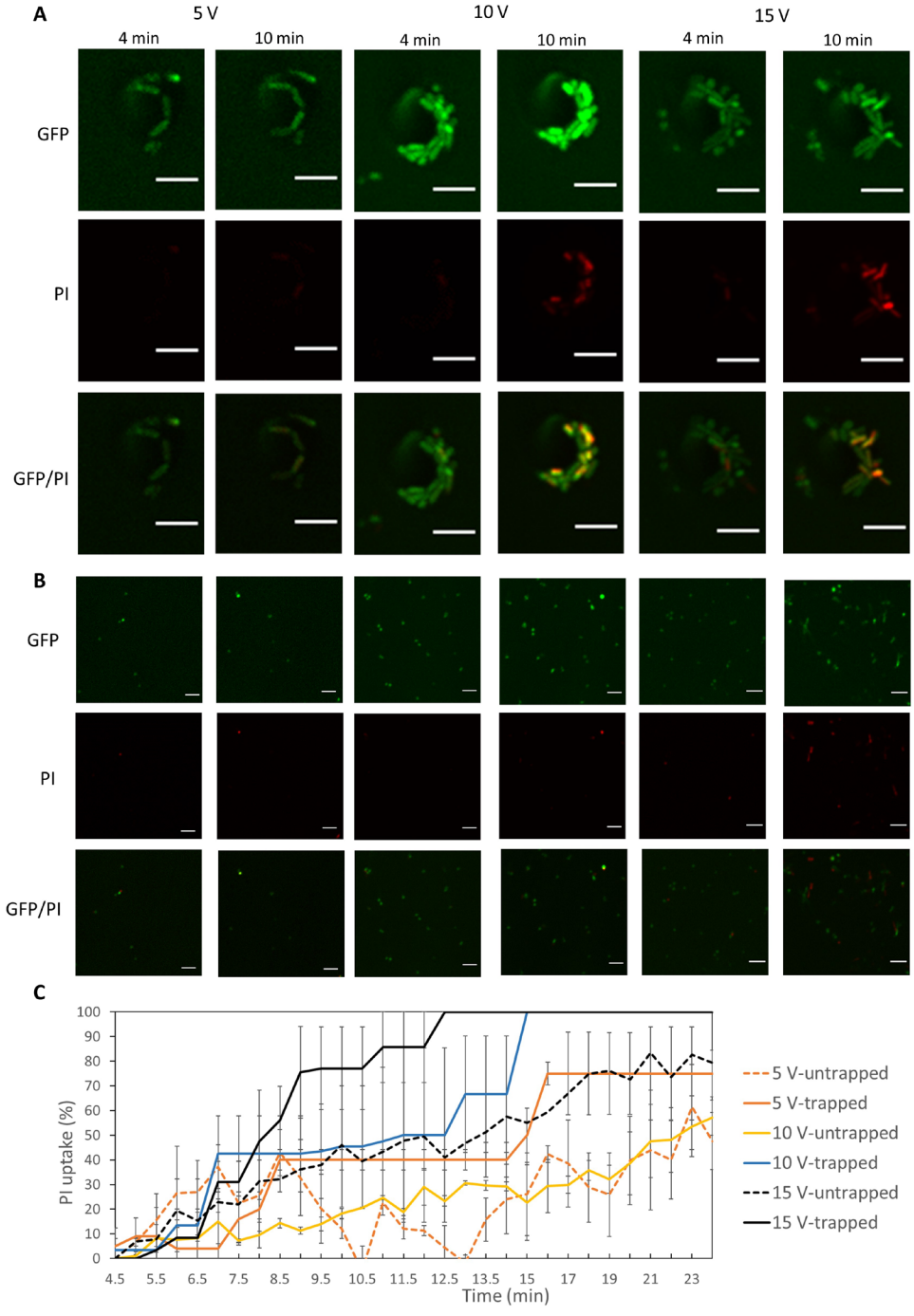

Fig. 4. Microscopy images of PI-stained trapped versus nontrapped *E. coli* at high frequency (5 MHz), various applied voltages, and operation times. PI uptake (red fluorescence) indicates cell electroporation. (**A**) Trapped and (**B**) untrapped *E. coli* are shown. (**C**) Percentage of both trapped and untrapped PI-stained *E. coli* at various applied voltages (5 MHz). Error bars represent SD computed from three independent tests. JP of 10 μm in diameter was used. Scale bars, 5 μm. *E. coli* strain XL1-Blue bacteria with GFP labeling were used.

restricted to a specific design of electrodes [i.e., mobile microelectrodes (e.g., JP) or fixed electrodes as in common chip designs], these mechanisms are generic also when combined together as demonstrated here using the active carrier. Specifically, although the DEP response [i.e., the Clausius-Mossotti factor (*13*)] of different cell types maybe different, it can be controlled by tuning the frequency to achieve the desired behavior (e.g., positive DEP as in the current study). The same applies for the electroporation where, by tuning the continuous AC field or train of pulse parameters (e.g., number, intensity, and duration), one can achieve desired electroporation conditions for different cell types. To further demonstrate its applicability to other types of bacteria, we performed an experiment with

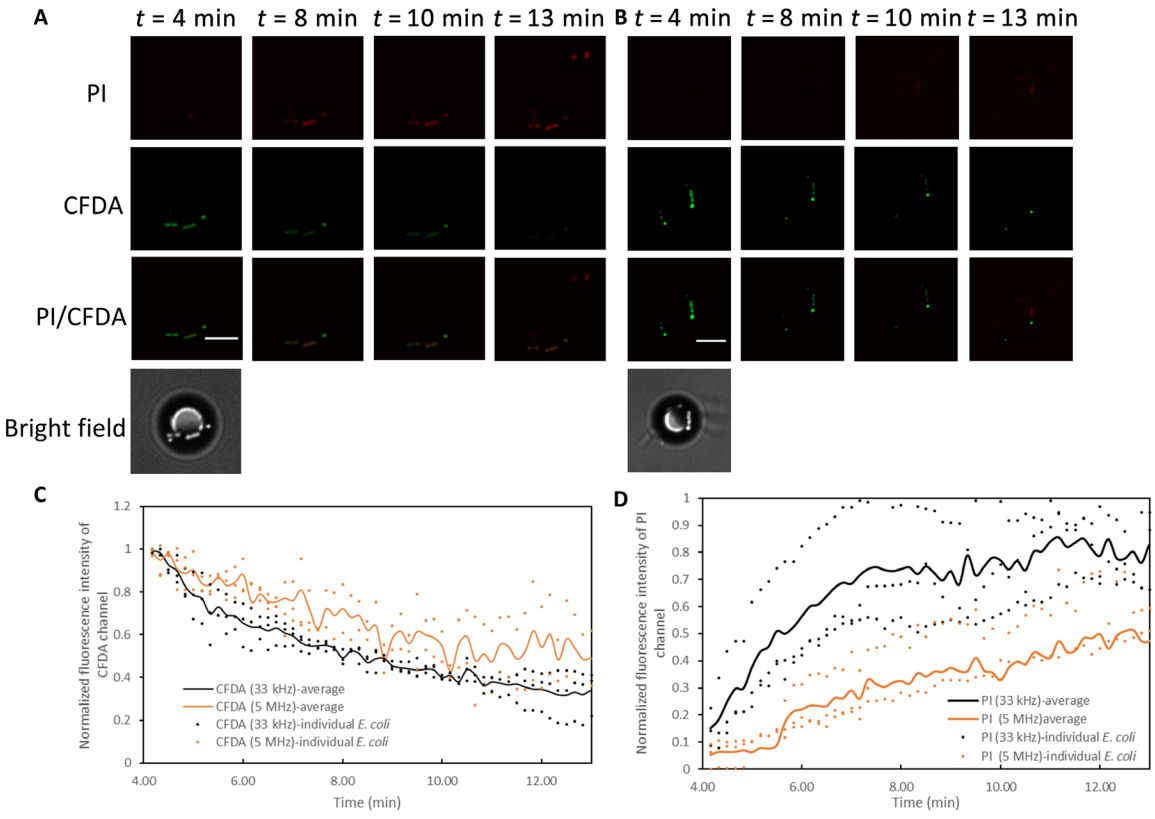

Fig. 5. Microscopy images of CFDA and PI-stained trapped *E. coli* at both low (33 kHz) and high (5 MHz) frequency, 10 V, and various operation times. CFDA (green fluorescence) indicates cell viability, and PI uptake (red fluorescence) indicates cell electroporation. (**A**) Low-frequency (33 kHz) and (**B**) high-frequency (5 MHz) trapped *E. coli*. (**C** and **D**) Normalized fluorescence intensity (i.e., ratio of the overall fluorescence intensity within a circle of 3 μm in diameter around each bacteria to its maximum overall fluorescence intensity value) of trapped *E. coli* in (C) CFDA channel and (D) PI channel for both low (33 kHz) and high (5 MHz) frequencies. Continuous lines represent averaged values of the individual bacteria depicted as points. JPs of 10 μm in diameter were used. Scale bars, 5 μm. *E. coli* strain XL1-Blue bacteria without GFP labeling were used.

Rhodococcus erythropolis ATCC (American Type Culture Collection) 4277 of spherical shape (unlike the rod shape of *E. coli*). As shown in fig. S4 (C and D), successful trapping and reversible electroporation of PI were achieved (>80% intake efficiency) for the trapped *Rhodococcus* without inducing notable cell damage, as revealed by ~50% CFDA retention when the electroporation is conducted at 33 kHz and 10 V for less than 2 min. As expected, the untrapped cells showed no significant PI uptake.

Together, the JP can be applied to preconcentrate and electroporate trace amounts of bacteria in samples, which can then be analyzed in a short time period. This application is important in water safety monitoring, health surveillance, and clinical diagnosis, where detection and identification of trace amounts of viable bacterial pathogens are in high demand (*42*). It is expected that the described biological cargo carrier and targeted electroporation can be used in applications integrating single-cell analysis methods, such as polymerase chain reaction, gene sequencing, fluorescence in situ hybridization, and immunofluorescence staining, where the carrier will selectively pick up a target and transport it to a secondary chamber to be lysed for further analysis of its genomics (*43*), transcriptomics (*44*), proteomics (*45*), or metabolomics (*46*). The selective trapping and single-cell lysis system also enable investigation of cell heterogeneity (*47*).

The observation that an AC pulse train can electroporate cells while keeping them trapped opens the opportunity of introducing large molecules and plasmid DNA into the bacteria, which can be of important utility in gene cloning and research of molecular biology (*48*). The JP can accurately trap the desired number of DNA plasmids to be transfected into the target cell. There is very limited literature addressing means of controlling the precise number of DNA plasmids to be electroporated into cells (including bacterial). Current transfection methods [cuvette and micropipette methods (*49*)] roughly control the amount of plasmid being transfected by controlling the bulk concentration of the plasmid.

The fact that the active particle achieved its highest velocity and positive DEP force in medium with low conductivities (<0.09 S/m) may require exchanging the physiological solution with solution of low ionic conductivity but of similar osmolality, when needed (e.g., mammalian cells). This exchange of buffer is commonly performed in standard electroporation procedures (*50*). For bacterial and yeast cells, the use of low-conductivity solution is not a limitation. It may also be solved for physiological medium conditions by combining a nonelectrokinetic propulsion mechanism (*7*, *10*, *51*), in combination with electrical-based DEP for manipulation (load and release) of the biological cargo and electroporation.

Similar to nanochannel electroporation (*52*), our mobile microelectrode is able to perform electroporation only on a smaller portion of the cell (i.e., minimally invasive in case of cells larger than the JP) and hence is expected to result in significantly higher reversible

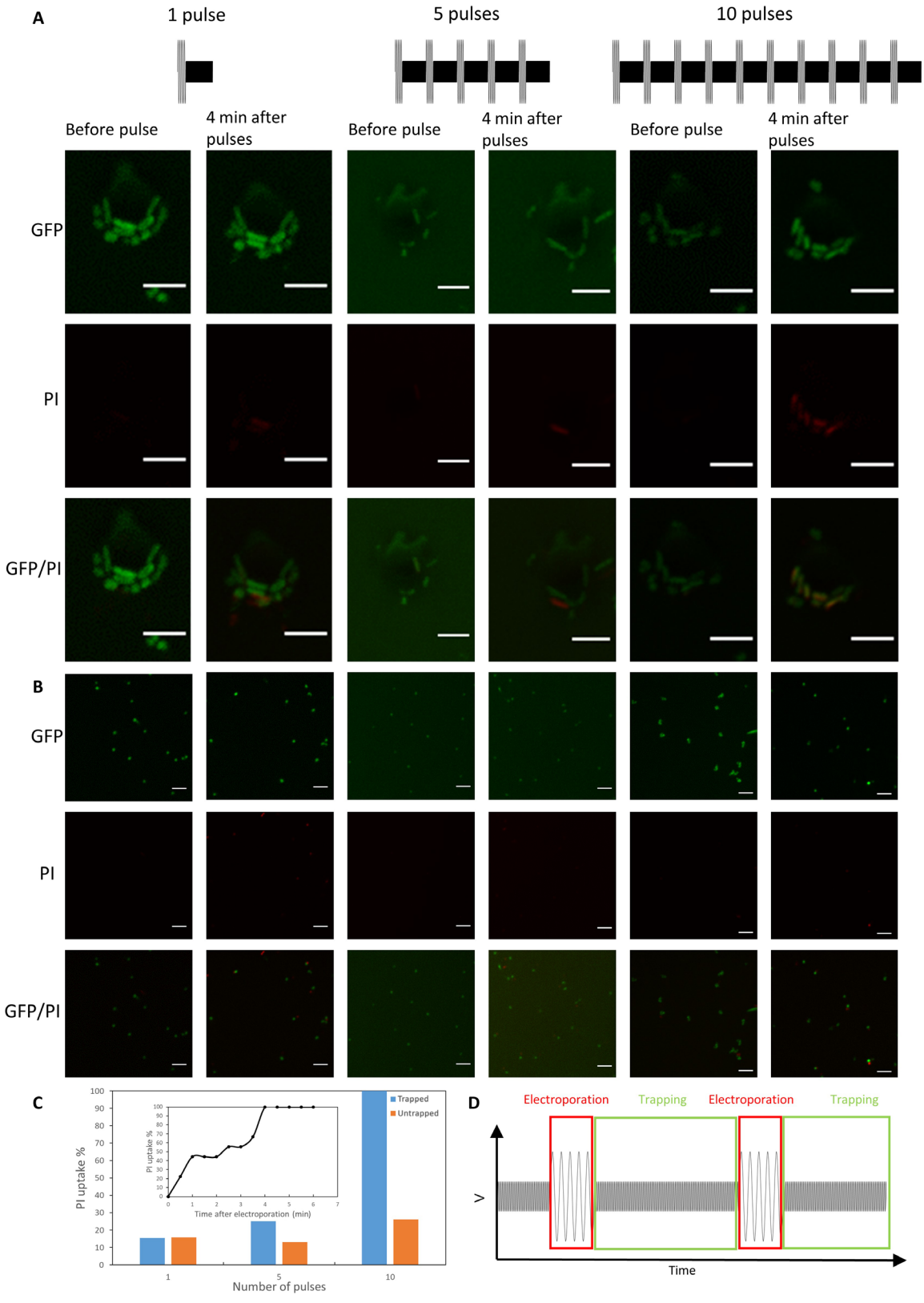

Fig. 6. Microscopy images of PI-stained trapped versus nontrapped *E. coli* under an AC pulse train, various number of pulses, and operation times. PI uptake (red fluorescence) indicates cell electroporation. (**A**) Trapped and (**B**) untrapped *E. coli*. (**C**) Percentage of both trapped and untrapped PI-stained *E. coli*, 4 min after pulses (frequency: 2 MHz; voltage: 10 V; duration: 0.5 ms). Inset: Percentage of PI-stained cells over time, following a train of 10 pulses. (**D**) Variation of AC voltage and frequency across the experiment chamber and over time. JP of 10 μm in diameter was used. *E. coli* strain XL1-Blue bacteria with GFP labeling were used. Scale bars, 5 μm.

electroporation yield, as the locally electroporated cells can be more easily recovered relative to standard electroporation. The latter not only is not selective, i.e., all bacteria in the chamber are uniformly electroporated, but also results in the entire cell membrane being electroporated because of the uniform electric field conditions on the cell membrane (*53*, *54*). Moreover, because of the ability to preconcentrate not only the targeted cells but also large molecules (e.g., plasmids) to be electroporated onto the same JP, the electroporation yield for the targeted cells (e.g., bacteria) should be increased substantially. In bacteria, there is also a cell wall in addition to cell membrane, where both are affected by the electric field (*55*). However, while small molecules (e.g., PI), introduced into the cell through the electroporated cell membrane, are not affected by the cell wall, large molecules (e.g., plasmids) are trapped within the cell wall (*48*, *55*).

Thus, the groundbreaking concept of a unified selective transport and electroporation using the mobile microelectrode–based micromotor described above enables the development of novel microscale and nanoscale tools for single-cell analysis and opens new opportunities for targeted delivery.

METHODS

Magnetic JP fabrication

Polystyrene particles (diameter: 10 μm) (Sigma-Aldrich) in isopropanol (IPA) were pipetted onto a glass microscope slide to form a monolayer of particles upon solvent evaporation. The glass slide was coated with 15-nm Cr, followed by 50-nm Ni and 15-nm Au, as described in the protocol outlined by Pethig (*14*) and Wu *et al.* (*56*). To magnetize the JPs, the substrates were placed in between two neodymium magnetic blocks (14 mm × 12 mm × 19 mm in size), with opposite dipoles facing each other. Next, the substrate was sonicated in deionized (DI) water with 2% (v/v) Tween 20 (Sigma-Aldrich) to release the JPs. The JPs were then washed three times in DI water with 0.01% (v/v) Tween 20 (Sigma-Aldrich) and 7×10^{-5} M KCl before the experiment.

Magnetic steering of JPs

JPs were guided by placing the neodymium magnet block (14 mm × 12 mm × 19 mm in size) at a specific orientation close to the microchamber (see fig. S5C). The magnet was kept at a horizontal distance of 3 cm from the focus of the objective and at the same height as the microchamber. In this setup, the magnet produced a field of 125 G in the microchamber.

Cell culture and preparation of bacteria solution

E. coli strain XL1-Blue bacteria were cultured at 37°C and 250 rpm in Luria-Bertani (LB) medium containing tryptone (10 g/liter), yeast extract (5 g/liter), and NaCl (10 g/liter). Electrocompetent cells were prepared when the cultures reach an OD_{600} (optical density at 600 nm) of 0.5 to 0.7 using a glycerol method and frozen in a −80°C freezer. To label bacteria with green fluorescent protein (GFP), a pCDNA3.1-GFP plasmid was transformed to XL1-Blue–competent cells by electroporation (1800 W, 0.5 ms). Cells were cultured in an LB agar plate with ampicillin resistance to grow as single colonies. Bacteria were picked up from a colony for experiments using a pipette tip and incubated for 5 min at room temperature in 200 μl of DI water, which contained PI (33 μg/ml), 0.01% (v/v) Tween 20 (Sigma-Aldrich), and 7×10^{-5} M KCl. To label the cell with CFDA, XL1-Blue bacteria (without GFP labeling) were cultured in an LB agar plate without ampicillin resistance to grow as single colonies. Bacteria were picked up from a colony for experiments using a pipette tip and incubated for 30 min at 37°C in 0.1 mM phosphate buffer [pH 8.5, 5% (w/v) NaCl, 0.5 mM EDTA disodium salt] and CFDA solution (10 mg/ml) according to the manufacturer's protocol. Cells were washed three times with DEP buffer [Hepes (2385 mg/liter), sucrose (80,700 mg/liter), and dextrose (4500 mg/liter)] (*57*). Before the experiment, PI (3 μg/ml) and 0.1% Tween 20 were added into the solution. Moreover, the conductivity was adjusted to 9 μS/cm by adding KCl and then incubated for 5 min at room temperature. All chemicals were purchased from Sigma-Aldrich.

R. erythropolis ATCC 4277 were cultured at 30°C in an LB agar plate for 48 hours to grow as single colonies. Bacteria were picked up from a colony for experiments using a pipette tip and incubated for 30 min at 30°C in phosphate-buffered saline with CFDA solution (10 mg/ml) according to the manufacturer's protocol. Cells were washed three times with DEP buffer [Hepes (2385 mg/liter), sucrose (80,700 mg/liter), and dextrose (4500 mg/liter)] (*57*). Before the experiment, PI (3 μg/ml) and 0.1% Tween 20 were added into the solution. Moreover, the conductivity was adjusted to 9 μS/cm by adding KCl and then incubated for 5 min at room temperature. All chemicals were purchased from Sigma-Aldrich.

Preparation of polystyrene tracer particle solution

For observation of electroconvection, a solution consisting of 0.01% (v/v) 720-nm-diameter polystyrene particles (Fluoro-Max) was prepared. Particles were rinsed three times with DI water, to which a small amount (0.01%, v/v) of nonionic surfactant (Tween 20; Sigma-Aldrich) and 7×10^{-5} M KCl were added to minimize adhesion to the ITO substrate before being injected into the microfluidic chamber via a small hole at the upper substrate, drilled expressly for this purpose.

Experimental setup

The experimental chamber consisted of a 120-μm-high, silicone reservoir (Grace Bio-Labs), sandwiched between an ITO-coated, 1-mm glass slide (Delta Technology) and an ITO-coated coverslip (SPI Systems), as illustrated by Boymelgreen *et al.* (*15*) (see fig. S1). Two inlet holes (~1 mm in diameter) were drilled through the top 1-mm ITO slide, surrounded by a silicone reservoir (2 mm in height and 9 mm in diameter) filled with solution, to ensure that the chamber remained wet and to enable the addition of the solution with the JPs, bacteria, fluorescent dyes, and tracer particles into the channel via manual pumping. The AC electrical forcing was applied using a signal generator (Agilent 33250A) and monitored with an oscilloscope (Tektronix TPS2024). An AC pulse signal was applied using a signal generator (TTi TGA 12104 series) with multiple channels. A laboratory-made switch [Solid State Relays (AQV252G) controlled by Arduino Nano] was used to control the duration and timing of AC pulses. A power amplifier (Falco System) was used to amplify the output signal.

Selective trapping of *E. coli* by JPs and electroporation

Active collection of *E. coli* was performed in the ITO chamber at 300 kHz and 10 V for 2 min. In the following 2 min, the electrical field parameters were changed to find the conditions (i.e., zero velocity of the JP) for the electroporation stage during which untrapped *E. coli* diffuse away. The remaining trapped *E. coli* underwent electroporation using either continuous AC signal for different amplitudes, frequencies, and durations, as depicted in Figs. 3A and 4A, or using

an AC pulse train under a continuous AC signal with a frequency of 5 MHz. The AC pulse train consisted of electroporation pulses (frequency: 33 kHz and 30 V; duration: 0.5 ms) with 1-s intervals of a continuously applied electric field (frequency: 2 MHz and 10 V) for trapping purposes.

Microscopy and image analysis

Trapped and untrapped *E. coli* (Figs. 3 to 6) were observed using a Nikon Eclipse Ti-E inverted microscope equipped with a Yokogawa CSU-X1 spinning disk confocal scanner and an Andor iXon-897 EMCCD camera. The chamber was placed with the coverslip side down, and images were taken using a 60× oil immersion lens. GFP and PI fluorescent dyes were observed with lasers of wavelengths 488 and 561 nm, respectively. If the cell shows 50% fluorescence intensity of its maximum value, then it was considered PI stained. The PI uptake (Figs. 3C, 4C, and 6C) was computed as the ratio between the number of PI-stained trapped *E. coli* and the total number of trapped *E. coli* after subtraction of the number of PI-stained *E. coli* at 4 min. Here, again, the bacteria trapped above the JP were not included.

Numerical simulations

The numerical simulation used to qualitatively verify the presence of asymmetric electric field gradients arising from the proximity of a Janus sphere near a conducting wall was performed in COMSOL 5.3. A simple two-dimensional geometry, consisting of a rectangular channel, 50 μm height and 100 μm width, with a 10-μm-diameter circle placed 300 nm above the substrate, was used to model the experimental setup. Because the EDLs are thin relative to the radius of the particle ($\lambda/a \ll 1$), within the electrolyte, we can solve the Laplace equation for the electric potential, ϕ, in conjunction with the following boundary condition at the metallic side of the JP

$$\sigma\frac{\partial\phi}{\partial n} = i\omega C_{DL}(\phi - V_{floating}) \quad (1)$$

which describes the oscillatory ohmic charging of the induced EDL, wherein $V_{floating}$ is the floating potential of the metallic hemisphere of the JP, n is the coordinate in the direction of the normal to the JP surface, and C_{DL} represents the capacitance per unit area of the EDL and may be estimated from the Debye-Hückel theory as $C_{DL} \sim \varepsilon/\lambda$. In addition, a floating boundary condition (*19*) was applied on the metallic hemisphere so as to obey total zero charge. An insulation boundary condition was applied on the dielectric hemisphere of the JP, a voltage of 6.25 V was applied at the lower substrate ($y = 0$), while the upper wall was grounded, and the edges of the channel were given an insulating boundary condition.

Calculation of the transmembrane potential

The following Schwan's equation (*39*) was used for the approximation of the transmembrane potential of *E. coli*:

$$\Delta\psi_{membr} = 1.5aE_{appl}\cos\theta/[1 + (\omega\tau)^2]^{1/2} \quad (2)$$

$$\tau = aC_{membr}\left(\rho_{int} + \frac{\rho_{ext}}{2}\right) \quad (3)$$

where θ is the angle between the electric field direction and the normal to the cell membrane, E_{appl} is the applied field strength, f is the frequency, $\omega = 2\pi f$ is the angular frequency, a is the radius of the cell, C_{membr} (F/cm^2) is the capacitance of the membrane, ρ_{int} is the resistivity of the internal fluid, ρ_{ext} is the resistivity of external medium, and τ is the membrane relaxation time. As an example, for applied voltage difference of 10 V, the calculated transmembrane potential is 0.1 and 0.002 V for frequencies of 33 kHz and 5 MHz, respectively (see table S1), demonstrating the decreased electroporation efficiency with an increasing frequency.

SUPPLEMENTARY MATERIALS

Supplementary material for this article is available at http://advances.sciencemag.org/cgi/content/full/6/5/eaay4412/DC1

Fig. S1. Positive DEP response of both CFDA [live (green fluorescent)] and PI-stained [dead (red fluorescent)] *E. coli* within a quadrupolar electrode array and a solution conductivity of 9 μS/cm.
Fig. S2. Polystyrene particles (2 μm) trapped under the metallic coated hemisphere of the JP under various voltages.
Fig. S3. JP (10 μm) path during the trapping process of *E. coli*, as obtained by superimposing microscope images at different times, operated under 10 V and 200 kHz.
Fig. S4. Microscopy images of PI- and CFDA-stained trapped versus nontrapped *Rhodococcus* at low frequency of 33 Hz, 10 V, and various operation times.
Fig. S5. Experimental setup.
Table S1. Parameters used for the calculation of the *E. coli* transmembrane potential.
Movie S1. JP velocity for different frequencies (10 kHz, 30 kHz, 300 kHz, and 5 M Hz) under 10 V.
Movie S2. Electroporation process using continuous AC signal of low frequency consisting of 2-min collection of *E. coli* (300 kHz and 10 V) under GFP channel, 22 min of electroporation (55 kHz and 10 V) under GFP, and PI and GFP/PI channels and release under PI channel.
Movie S3. Electroporation process using continuous AC signal of high frequency consisting of 2-min collection of *E. coli* (300 kHz and 10 V) under GFP optical channel, 22 min of electroporation (5 MHz and 15 V) under GFP, and PI and GFP/PI channels and release under PI channel.
Movie S4. Electroconvection around the JP visualized using 720-nm polystyrene particles as tracers.
Movie S5. Electroporation process using a train of AC pulses consisting of 2-min collection of *E. coli* (300 kHz and 10 V) under GFP channel, a train of sinusoidal AC pulses (number of pulse: 10 pulses; pulse duration: 0.5 ms; frequency: 30 kHz; amplitude: 30 V) for electroporation under GFP channel, 4-min holding (2 MHz and 10 V), and observing PI uptake under GFP, PI, and GFP/PI channels and release under PI channel.

REFERENCES AND NOTES

1. W. Gao, R. Dong, S. Thamphiwatana, J. Li, W. Gao, L. Zhang, J. Wang, Artificial micromotors in the mouse's stomach: A step toward *in vivo* use of synthetic motors. *ACS Nano* **9**, 117–123 (2015).
2. J. Orozco, G. Cheng, D. Vilela, S. Sattayasamitsathit, R. Vazquez-Duhalt, G. Valdés-Ramírez, O. S. Pak, A. Escarpa, C. Kan, J. Wang, Micromotor-based high-yielding fast oxidative detoxification of chemical threats. *Angew. Chem. Int. Ed.* **52**, 13276–13279 (2013).
3. W. Gao, X. Feng, A. Pei, Y. Gu, J. Li, J. Wang, Seawater-driven magnesium based Janus micromotors for environmental remediation. *Nanoscale* **5**, 4696–4700 (2013).
4. J. Li, O. E. Shklyaev, T. Li, W. Liu, H. Shum, I. Rozen, A. C. Balazs, J. Wang, Self-propelled nanomotors autonomously seek and repair cracks. *Nano Lett.* **15**, 7077–7085 (2015).
5. K. Han, C. W. Shields IV, O. D. Velev, Engineering of self-propelling microbots and microdevices powered by magnetic and electric fields. *Adv. Funct. Mater.* **28**, 1705953 (2018).
6. S. Gangwal, O. J. Cayre, M. Z. Bazant, O. D. Velev, Induced-charge electrophoresis of metallodielectric particles. *Phys. Rev. Lett.* **100**, 058302 (2008).
7. Z. Wu, J. Troll, H.-H. Jeong, Q. Wei, M. Stang, F. Ziemssen, Z. Wang, M. Dong, S. Schnichels, T. Qiu, P. Fischer, A swarm of slippery micropropellers penetrates the vitreous body of the eye. *Sci. Adv.* **4**, eaat4388 (2018).
8. Y. Wu, T. Si, J. Shao, Z. Wu, Q. He, Near-infrared light-driven Janus capsule motors: Fabrication, propulsion, and simulation. *Nano Res.* **9**, 3747–3756 (2016).
9. T. Xu, W. Gao, L.-P. Xu, X. Zhang, S. Wang, Fuel-free synthetic micro-/nanomachines. *Adv. Mater.* **29**, 1603250 (2017).
10. T. Mirkovic, N. S. Zacharia, G. D. Scholes, G. A. Ozin, Nanolocomotion—Catalytic nanomotors and nanorotors. *Small* **6**, 159–167 (2010).
11. S. Sundararajan, P. E. Lammert, A. W. Zudans, V. H. Crespi, A. Sen, Catalytic motors for transport of colloidal cargo. *Nano Lett.* **8**, 1271–1276 (2008).
12. J. Orozco, S. Campuzano, D. Kagan, M. Zhou, W. Gao, J. Wang, Dynamic isolation and unloading of target proteins by aptamer-modified microtransporters. *Anal. Chem.* **83**, 7962–7969 (2011).
13. A. M. Boymelgreen, T. Balli, T. Miloh, G. Yossifon, Active colloids as mobile microelectrodes for unified label-free selective cargo transport. *Nat. Commun.* **9**, 760 (2018).

14. R. Pethig, Review—Where is dielectrophoresis (DEP) going? *J. Electrochem. Soc.* **164**, B3049–B3055 (2017).
15. A. Boymelgreen, G. Yossifon, T. Miloh, Propulsion of active colloids by self-induced field gradients. *Langmuir* **32**, 9540–9547 (2016).
16. N. L. Abbott, O. D. Velev, Active particles propelled into researchers' focus. *Curr. Opin. Colloid Interface Sci.* **21**, 1–3 (2016).
17. S. J. Ebbens, Active colloids: Progress and challenges towards realising autonomous applications. *Curr. Opin. Colloid Interface Sci.* **21**, 14–23 (2016).
18. J. Yan, M. Han, J. Zhang, C. Xu, E. Luijten, S. Granick, Reconfiguring active particles by electrostatic imbalance. *Nat. Mater.* **15**, 1095–1099 (2016).
19. T. M. Squires, M. Z. Bazant, Breaking symmetries in induced-charge electro-osmosis and electrophoresis. *J. Fluid Mech.* **560**, 65–101 (2006).
20. A. F. Demirörs, M. T. Akan, E. Poloni, A. R. Studart, Active cargo transport with Janus colloidal shuttles using electric and magnetic fields. *Soft Matter* **14**, 4741–4749 (2018).
21. R. B. Brown, J. Audet, Current techniques for single-cell lysis. *J. R. Soc. Interface* **5**, S131–S138 (2008).
22. M. Hügle, G. Dame, O. Behrmann, R. Rietzel, D. Karthe, F. T. Hufert, G. A. Urban, A lab-on-a-chip for preconcentration of bacteria and nucleic acid extraction. *RSC Adv.* **8**, 20124–20130 (2018).
23. P. Vulto, G. Dame, U. Maier, S. Makohliso, S. Podszun, P. Zahn, G. A. Urban, A microfluidic approach for high efficiency extraction of low molecular weight RNA. *Lab Chip* **10**, 610–616 (2010).
24. J. Olofsson, K. Nolkrantz, F. Ryttsén, B. A. Lambie, S. G. Weber, O. Orwar, Single-cell electroporation. *Curr. Opin. Biotechnol.* **14**, 29–34 (2003).
25. C. Xie, Z. Lin, L. Hanson, Y. Cui, B. Cui, Intracellular recording of action potentials by nanopillar electroporation. *Nat. Nanotechnol.* **7**, 185–190 (2012).
26. H. Lu, M. A. Schmidt, K. F. Jensen, A microfluidic electroporation device for cell lysis. *Lab Chip* **5**, 23–29 (2005).
27. L. Chang, M. Howdyshell, W.-C. Liao, C.-L. Chiang, D. Gallego-Perez, Z. Yang, W. Lu, J. C. Byrd, N. Muthusamy, L. J. Lee, R. Sooryakumar, Magnetic tweezers-based 3D microchannel electroporation for high-throughput gene transfection in living cells. *Small* **11**, 1818–1828 (2015).
28. L. Chang, D. Gallego-Perez, X. Zhao, P. Bertani, Z. Yang, C.-L. Chiang, V. Malkoc, J. Shi, C. K. Sen, L. Odonnell, J. Yu, W. Lu, L. J. Lee, Dielectrophoresis-assisted 3D nanoelectroporation for non-viral cell transfection in adoptive immunotherapy. *Lab Chip* **15**, 3147–3153 (2015).
29. J. A. Lundqvist, F. Sahlin, M. A. I. Åberg, A. Strömberg, P. S. Eriksson, O. Orwar, Altering the biochemical state of individual cultured cells and organelles with ultramicroelectrodes. *Proc. Natl. Acad. Sci. U.S.A.* **95**, 10356–10360 (1998).
30. B. P. Nadappuram, P. Cadinu, A. Barik, A. J. Ainscough, M. J. Devine, M. Kang, J. Gonzalez-Garcia, J. T. Kittler, K. R. Willison, R. Vilar, P. Actis, B. Wojciak-Stothard, S.-H. Oh, A. P. Ivanov, J. B. Edel, Nanoscale tweezers for single-cell biopsies. *Nat. Nanotechnol.* **14**, 80–88 (2019).
31. E. N. Tóth, A. Lohith, M. Mondal, J. Guo, A. Fukamizu, N. Pourmand, Single-cell nanobiopsy reveals compartmentalization of mRNAs within neuronal cells. *J. Biol. Chem.* **293**, 4940–4951 (2018).
32. S. Homhuan, B. Zhang, F.-S. Sheu, A. A. Bettiol, F. Watt, Single-cell electroporation using proton beam fabricated biochips. *Biomed. Microdevices* **14**, 533–540 (2012).
33. H. Sedgwick, F. Caron, P. B. Monaghan, W. Kolch, J. M. Cooper, Lab-on-a-chip technologies for proteomic analysis from isolated cells. *J. R. Soc. Interface* **5** (suppl. 2), S123–S130 (2008).
34. C. Lyu, J. Wang, M. Powell-Palm, B. Rubinsky, Simultaneous electroporation and dielectrophoresis in non-electrolytic micro/nano-electroporation. *Sci. Rep.* **8**, 2481 (2018).
35. A. Boymelgreen, G. Yossifon, Observing electrokinetic Janus particle–channel wall interaction using microparticle image velocimetry. *Langmuir* **31**, 8243–8250 (2015).
36. D. Ben-Bassat, A. Boymelgreen, G. Yossifon, The influence of flow intensity and field frequency on continuous-flow dielectrophoretic trapping. *J. Colloid Interface Sci.* **442**, 154–161 (2015).
37. T. Batista Napotnik, D. Miklavčič, In vitro electroporation detection methods – An overview. *Bioelectrochemistry* **120**, 166–182 (2018).
38. E. Neumann, A. E. Sowers, C. A. Jordan, *Electroporation and Electrofusion in Cell Biology* (Springer US, Boston, MA, 1989).
39. P. Marszalek, D.-S. Liu, T. Y. Tsong, Schwan equation and transmembrane potential induced by alternating electric field. *Biophys. J.* **58**, 1053–1058 (1990).
40. A. Baumstummler, R. Chollet, H. Meder, F. Olivieri, S. Rouillon, G. Waiche, S. Ribault, Development of a nondestructive fluorescence-based enzymatic staining of microcolonies for enumerating bacterial contamination in filterable products. *J. Appl. Microbiol.* **110**, 69–79 (2011).
41. Y. Zhan, Z. Cao, N. Bao, J. Li, J. Wang, T. Geng, H. Lin, C. Lu, Low-frequency ac electroporation shows strong frequency dependence and yields comparable transfection results to dc electroporation. *J. Control. Release* **160**, 570–576 (2012).
42. L. Wu, T. Luan, X. Yang, S. Wang, Y. Zheng, T. Huang, S. Zhu, X. Yan, Trace detection of specific viable bacteria using tetracysteine-tagged bacteriophages. *Anal. Chem.* **86**, 907–912 (2014).
43. F. Lan, B. Demaree, N. Ahmed, A. R. Abate, Single-cell genome sequencing at ultra-high-throughput with microfluidic droplet barcoding. *Nat. Biotechnol.* **35**, 640–646 (2017).
44. R. J. Kimmerling, G. Lee Szeto, J. W. Li, A. S. Genshaft, S. W. Kazer, K. R. Payer, J. de Riba Borrajo, P. C. Blainey, D. J. Irvine, A. K. Shalek, S. R. Manalis, A microfluidic platform enabling single-cell RNA-seq of multigenerational lineages. *Nat. Commun.* **7**, 10220 (2016).
45. R. D. Pedde, H. Li, C. H. Borchers, M. Akbari, Microfluidic-mass spectrometry interfaces for translational proteomics. *Trends Biotechnol.* **35**, 954–970 (2017).
46. L. J. Barkal, A. B. Theberge, C.-J. Guo, J. Spraker, L. Rappert, J. Berthier, K. A. Brakke, C. C. C. Wang, D. J. Beebe, N. P. Keller, E. Berthier, Microbial metabolomics in open microscale platforms. *Nat. Commun.* **7**, 10610 (2016).
47. W. Jing, B. Camellato, I. J. Roney, M. Kaern, M. Godin, Measuring single-cell phenotypic growth heterogeneity using a microfluidic cell volume sensor. *Sci. Rep.* **8**, 17809 (2018).
48. M. Kandušer, D. Miklavčič, *Electroporation in Biological Cell and Tissue: An Overview* (Springer, 2009), pp. 1–37.
49. J. S. Wiegert, C. E. Gee, T. G. Oertner, Single-cell electroporation of neurons. *Cold Spring Harb. Protoc.* **2017**, 135–138 (2017).
50. P. Ruzgys, M. Jakutavičiūtė, I. Šatkauskienė, K. Čepurnienė, S. Šatkauskas, Effect of electroporation medium conductivity on exogenous molecule transfer to cells in vitro. *Sci. Rep.* **9**, 1436 (2019).
51. Y.-L. Chen, C.-X. Yang, H.-R. Jiang, Electrically enhanced self-thermophoresis of laser-heated Janus particles under a rotating electric field. *Sci. Rep.* **8**, 5945 (2018).
52. K. Gao, L. Li, L. He, K. Hinkle, Y. Wu, J. Ma, L. Chang, X. Zhao, D. G. Perez, S. Eckardt, J. Mclaughlin, B. Liu, D. F. Farson, L. J. Lee, Design of a microchannel-nanochannel-microchannel array based nanoelectroporation system for precise gene transfection. *Small* **10**, 1015–1023 (2014).
53. D. C. Chang, T. S. Reese, Changes in membrane structure induced by electroporation as revealed by rapid-freezing electron microscopy. *Biophys. J.* **58**, 1–12 (1990).
54. J. F. Miller, W. J. Dower, L. S. Tompkins, High-voltage electroporation of bacteria: Genetic transformation of Campylobacter jejuni with plasmid DNA. *Proc. Natl. Acad. Sci. U.S.A.* **85**, 856–860 (1988).
55. H. Kimoto, A. Taketo, Initial stage of DNA-electrotransfer into *E. coli* cells. *J. Biochem.* **122**, 237–242 (1997).
56. C.-Y. Wu, K. T. Roybal, E. M. Puchner, J. Onuffer, W. A. Lim, Remote control of therapeutic T cells through a small molecule-gated chimeric receptor. *Science* **350**, aab4077 (2015).
57. S. V. Puttaswamy, S. Sivashankar, R.-J. Chen, C.-K. Chin, H.-Y. Chang, C. H. Liu, Enhanced cell viability and cell adhesion using low conductivity medium for negative dielectrophoretic cell patterning. *Biotechnol. J.* **5**, 1005–1015 (2010).

Acknowledgments: We thank the laboratory of A. Ciechanover for providing *E. coli* (XL1-Blue strain). We thank Y. Kashi for providing *R. erythropolis* ATCC 4277. We also thank E. Abraham and S. Wais for constructing the switch [Solid State Relays (AQV252G) controlled by Arduino Nano]. We thank N. Leibowitz for assistance with the numerical simulations. **Funding:** G.Y. acknowledges support from the Israel Science Foundation (ISF) (1938/16). Y.W. acknowledges support from the Technion-Guangdong project for postdoctoral fellowship. Fabrication of the chip was made possible through the financial and technical support of the Russell Berrie Nanotechnology Institute and the Micro-Nano Fabrication Unit. **Author contributions:** G.Y. and Y.W. created the concepts, designed the mechanism, performed the data analyses, and led the project. Y.W. performed the experiments and data analyses. A.F. and Y.W. prepared bacteria solution, cell staining, cell culturing, and extraction. G.Y. performed the simulations. G.Y. supervised the authors. All authors contributed to the writing of the manuscript. **Competing interests:** G.Y. and Y.W. are inventors on a patent/patent application related to this work filed by the Technion-I.I.T. (no. 07035-P0133A, filed on 17 March 2019). The authors declare that they have no other competing interests. **Data and materials availability:** All data needed to evaluate the conclusions in the paper are present in the paper and/or the Supplementary Materials. Additional data related to this paper may be requested from the authors.

Submitted 18 June 2019
Accepted 22 November 2019
Published 29 January 2020
10.1126/sciadv.aay4412

Citation: Y. Wu, A. Fu, G. Yossifon, Active particles as mobile microelectrodes for selective bacteria electroporation and transport. *Sci. Adv.* **6**, eaay4412 (2020).